Electrical and thermal conductivity of low temperature CVD graphene: the effect of disorder

2011 Nanotechnology 22 275716

(http://iopscience.iop.org/0957-4484/22/27/275716)

Nanotechnology **22** (2011) 275716 (9pp) doi:10.1088/0957-4484/22/27/275716

Electrical and thermal conductivity of low temperature CVD graphene: the effect of disorder

Ivan Vlassiouk[1], Sergei Smirnov[2], Ilia Ivanov[3], Pasquale F Fulvio[4], Sheng Dai[4], Harry Meyer[5], Miaofang Chi[5], Dale Hensley[3], Panos Datskos[1] and Nickolay V Lavrik[3]

[1] Measurement Science and System Engineering Division, Oak Ridge National Laboratory, Oak Ridge, TN 37931, USA
[2] Department of Chemistry and Biochemistry, New Mexico State University, Las Cruces, NM 88003, USA
[3] Center for Nanophase Materials Sciences, Oak Ridge National Laboratory, Oak Ridge, TN 37831, USA
[4] Chemical Sciences Division, Oak Ridge National Laboratory, Oak Ridge, TN 37831, USA
[5] Materials Science and Technology Division, Oak Ridge National Laboratory, Oak Ridge, TN 37831, USA

E-mail: vlassioukiv@ornl.gov

Received 20 February 2011, in final form 5 May 2011
Published 25 May 2011
Online at stacks.iop.org/Nano/22/275716

Abstract
In this paper we present a study of graphene produced by chemical vapor deposition (CVD) under different conditions with the main emphasis on correlating the thermal and electrical properties with the degree of disorder. Graphene grown by CVD on Cu and Ni catalysts demonstrates the increasing extent of disorder at low deposition temperatures as revealed by the Raman peak ratio, I_G/I_D. We relate this ratio to the characteristic domain size, L_a, and investigate the electrical and thermal conductivity of graphene as a function of L_a. The electrical resistivity, ρ, measured on graphene samples transferred onto SiO_2/Si substrates shows linear correlation with L_a^{-1}. The thermal conductivity, K, measured on the same graphene samples suspended on silicon pillars, on the other hand, appears to have a much weaker dependence on L_a, close to $K \sim L_a^{1/3}$. It results in an apparent $\rho \sim K^3$ correlation between them. Despite the progressively increasing structural disorder in graphene grown at lower temperatures, it shows remarkably high thermal conductivity (10^2–10^3 W K^{-1} m^{-1}) and low electrical (10^3–3×10^5 Ω) resistivities suitable for various applications.

S Online supplementary data available from stacks.iop.org/Nano/22/275716/mmedia

(Some figures in this article are in colour only in the electronic version)

1. Introduction

Since its introduction to broad research [1] graphene has quickly adopted the status of a wonder nanomaterial and has continued to draw the attention of an increasing number of researchers due to its unique properties [2–5]. Despite the well-recognized potential of graphene for numerous applications, a reliable technology for graphene scaled-up production remains a bottleneck in the transitioning from research to development of practically viable devices. Recent advances in chemical vapor deposition (CVD) growth [6], chemical techniques based on reduction of graphene oxide [2], and exfoliation in various solvents [7] appear promising in providing the routes for the desired high throughput synthesis of graphene. However, the quality of graphene synthesized by these methods strongly depends on the synthesis conditions and thus requires thorough optimization. Currently, CVD growth of graphene usually is performed at 1000 °C. Synthesis temperature reduction can substantially simplify the growth process, but preparing graphene via lowering the temperature of CVD

Table 1. Graphene used in this work.

Graphene type	Catalyst	Carbon source	T (°C)	I_G/I_D, 633 nm
Ni-830	Ni (∼8 graphene layers)	C_2H_2	830 ± 25	3–8 (4)
Cu-1000	Cu	CH_4	1000	3–13 (4)
Cu-830	Cu	C_2H_2	830 ± 25	∼1[a]
Cu-750	Cu	C_2H_2	750 ± 25	∼1[a]

[a] Even though the I_G/I_D ratios are similar for graphene Cu-830 and Cu-750, the amount of disorder is different (see figure 1). The uncertainty in the I_G/I_D ratio for Ni-830 and Cu-1000 represents variation throughout the sample including suspended samples; the ratio used in the analysis is shown in brackets.

leads to increasing contribution of defects that eventually become detrimental to its physical properties. In this paper we present a study of graphene produced by CVD on Ni and Cu substrates under various growth conditions with the main emphasis on correlating graphene's thermal and electrical properties with the degree of structural disorder due to low temperature deposition. Such correlation provides valuable information for the construction of various thermoelectric devices and provides guidance for thermal management applications requiring simultaneous control over electrical and thermal conductivities. Graphene samples were shown to have progressively increasing degree of structural disorder with lowering the temperature of CVD synthesis. Nevertheless, technologically attractive low temperature CVD graphene possesses very high electrical (10^2–10^3 W K^{-1} m^{-1}) and thermal (3×10^{-6}–10^{-3} Ω^{-1}) conductivities.

The CVD synthesis of graphene that we employ here can be performed on either Ni or Cu catalytic substrates. Because of a low carbon solubility in copper, graphene grows on Cu catalyst almost exclusively as a single layer; however, growth temperatures greater than 1000 °C are required for synthesis of high-quality graphene on Cu [6–11]. A Ni catalyst facilitates growth of well-ordered graphene at lower temperatures but, due to high carbon solubility, multiple graphene layers are usually produced with the reaction time and the cooling rate allowing some control over the number of produced graphene layers [12]. In this study we employed CVD of graphene on both Ni and Cu according to the protocols described in detail in the supplementary data (available at stacks.iop.org/Nano/22/275716/mmedia). We used four different synthetic routes summarized in table 1. We will refer to graphene grown on Ni at 830 °C and graphene grown on Cu at different temperatures (750–1000 °C) as, Ni-830, Cu-1000, Cu-830, and Cu-750 graphenes, where the numbers denote the synthesis temperature (table 1). The results reported here were reproduced multiple times on four Si wafers with 500–1000 nm SiO_2 and a 300–500 nm layer of metal catalyst. The majority of measurements were performed within a few days after synthesis but no noticeable deterioration was observed within weeks at ambient conditions.

2. Results and discussion

2.1. Raman characterization

Among different methods of characterizing the quality of CVD grown graphene, Raman spectroscopy is particularly useful as it is very sensitive to various kinds of defects and relatively well understood due to the rich history of its application in studying carbonaceous materials [13]. It will be our primary reference to quantify the degree of disorder in graphene, as other techniques (transmission electron microscopy (TEM), scanning electron microscopy (SEM), atomic force microscopy (AFM), x-ray photoelectron spectroscopy (XPS), Auger, optical) show a continuous monolayer for graphene synthesized on Cu with less obvious features for quality assessment.

The three major bands in the Raman spectra of graphene include the G band around 1580 cm^{-1} that corresponds to doubly degenerate E_{2g} optical phonon excitation and is always observed while the D band appearing near ∼1300 cm^{-1} attributed to the breathing mode increases in intensity with the number of defects breaking the symmetry, for example, near the graphene edges; and the most intense (for the visible light excitation) 2D (or G′) band in pristine graphene located near ∼2700 cm^{-1}. The latter band is an overtone of D and is associated with the same intervalley process but—in contrast to D—the defects are not required for its activation [13, 16–18]. A high ratio of 2D to G band intensities, $I_{2D}/I_G > 1$, along with a pure Lorentzian shape of 2D is considered a fingerprint of pristine graphene [19]. The relative intensity of 2D band is sensitive to environment and is typically less in the case of graphene on a substrate compared to suspended samples and is also significantly suppressed in multilayer graphene [19]. The I_{2D}/I_G intensity, positions, and width depends on the doping level and charged impurities [20, 21], which makes it tricky to use the I_{2D}/I_G ratio in evaluating the graphene quality. The I_D/I_G ratio, on the other hand, is less ambiguous in that regard and, as we show here, can be employed in optimizing the CVD growth conditions.

Figure 1 shows a set of representative Raman spectra of graphene samples transferred onto SiO_2/Si (left panel) and suspended on silicon pillars (right panel). Ni-830 graphene consists of approximately eight atomic layers on average, as estimated by the optical absorbance and supported by the XPS data (supplementary data available at stacks.iop.org/Nano/22/275716/mmedia). The magnitude of optical absorbances of graphene types Cu-750, 830, and 1000 measured in the visible range is very similar to that of the pristine graphene, i.e. $\pi e^2/\hbar c$ [14]. Confirmation of the single layer graphene on Cu also follows from the Lorentzian shape of the Raman peaks.

The Raman spectrum for Cu-1000 in figure 1 (left panel) shows pronounced features of a high-quality CVD graphene such as a high I_{2D}/I_G ratio, a narrow (∼30 cm^{-1} FWHM) 2D peak of the Lorentzian shape, and a relatively low intensity of

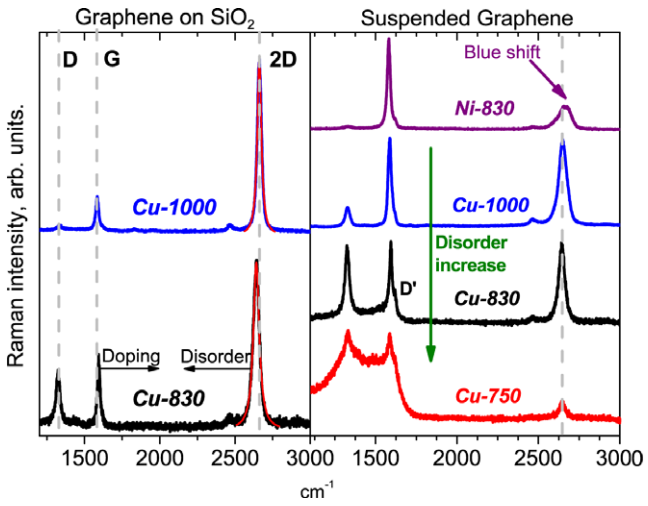

Figure 1. Representative Raman spectra of CVD graphene used in this study. Left panel: graphene transferred onto a SiO_2 substrate. (Cu-1000)—high quality Cu-1000 single layer CVD graphene; (Cu-830)—graphene Cu-830 with defects. 2D band fit to the Lorentzian lineshape is shown by the red line. Please note that for graphene Cu-830, the G line is stiffer and the 2D line is shifted toward the lower energies presumably due to Fermi energy increase induced by n-dopants and structural disorder [21, 22]. Spectra were normalized to have equal 2D line intensity. Right panel: suspended graphene over silicon pillars. (Ni-830)—CVD grown few layer graphene on Ni catalyst, Cu-1000, Cu-830, Cu-750—CVD grown graphene on Cu catalyst at 1000, 830, and 7500 °C. Spectra are normalized to the same G line intensity.

the D band. The I_{2D}/I_G ratio declines for suspended samples which likely indicates a stronger doping since both sides of this suspended graphene were exposed to wet chemistry (right panel). On the other hand, the I_D/I_G ratio remains nearly the same for each type of graphene sample regardless of whether it is suspended or not (left versus right panel in figure 1). The I_D/I_G ratio varies significantly between the samples and can be used for characterizing the degree of structural disorder in them [15]. For example, Cu-830 corresponds to graphene grown at a lower temperature and, as expected, is characterized by enhancement of the D band due to increased number of defects. The D band intensity increases even more for the Cu-750 sample prepared at the lowest temperature. One can notice other spectral changes with lowering the CVD temperature: decrease of the I_{2D}/I_G ratio, stiffening of G band, and slight softening of the 2D band and its broadening. Some of these changes can be attributed to an increased free charge carrier density [22] but the major contributor, especially with respect to the I_D/I_G ratio, is increased graphene disorder [23]. This conclusion is based on the fact that all samples were subjected to the same treatment during preparation and transfer and thus should have very similar doping levels. Nevertheless, the I_D/I_G ratio differs among them and decreases with lowering the temperature of growth, i.e. with increasing the degree of disorder. While increasing disorder can induce doping, for example due to the presence of five and seven cycles that may play the role of donors and acceptors, its contribution to the total doping is expected to be negligible unless there is preferential formation of a particular defect type.

Structural disorder in graphene manifests itself as a varying I_D/I_G intensity ratio in the Raman spectra and can be related to the characteristic size of well-ordered graphene domains, L_a. It was shown previously that the experimental correlation [16, 24, 25]:

$$L_a\ (\text{nm}) = \frac{560}{E_l^4}\frac{I_G}{I_D} \tag{1}$$

works well down to $L_a \sim 2$ nm ($I_G/I_D \sim 1$), where E_l—is the energy of the excitation photon in eV. When applied to our samples, equation (1) produces values of $L_a = 150 \pm 75$ and 38 ± 19 nm of Cu-1000 and Cu-830, respectively. The I_G/I_D ratio passes through a maximum at smaller L_a with a new correlation, $\frac{I_G}{I_D} \approx 1.8/L_a^2$ (for 514 nm excitation, L_a in nanometer) as described in [17]. This leads to $L_a = 1.3 \pm 0.7$ nm for the most disordered sample Cu-750, which is very close to that in carbon films ($L_a \sim 1.3$ nm) obtained by pyrolysis of an organic self-assembled monolayer [26].

2.2. Resistivity

The bulk resistivity and sheet resistance for 2D materials differ by the monolayer thickness and we will use them interchangeably. The resistivity, ρ, of the same types of graphene samples transferred onto SiO_2 was measured by the four point probe technique (supplementary data available at stacks.iop.org/Nano/22/275716/mmedia). The results are given in figure 2 along with literature data [27, 28, 9]. All data are plotted as a function of the degree of disorder expressed as I_G/I_D ratio (top axis) and L_a (bottom axis). It is clear that increasing disorder causes higher resistivity—all data show a good inverse correlation with L_a:

$$\rho = \frac{6.7 \times 10^{-4}}{L_a}. \tag{2}$$

The black line in figure 2, representing this dependence, also fits reasonably well the data reported previously for exfoliated and CVD grown graphene (open squares) [27, 28, 9] and even that of thin carbon films (light blue open square) obtained by pyrolysis of organic self-assembled monolayers [26]. The value of $L_a \sim 1.3$ nm for the latter was estimated from the Raman I_G/I_D intensity ratio, as described above. Data for pristine mechanically exfoliated graphene show large uncertainties along both axes due to a combination of difficult-to-control factors. For example, the Raman I_D/I_G ratio varies over an exfoliated graphene sample and is the largest at the edges. The value of $L_a \sim 1.7$ μm was estimated based on experimentally measured $I_D/I_G \sim 0.01$ (at 514 nm excitation) in the middle of large samples, which was also reported to vary significantly [27].

Given that even pristine graphene shows an experimentally detectable D band [27], one may argue that there are various chemical and physical imperfections present even in 'pristine' samples that affect their electrical and thermal conductivity. Charged surface impurities, resonant scatters, and strain/ripples have been proposed as the effectors of pristine graphene resistivity. They can alter the charge

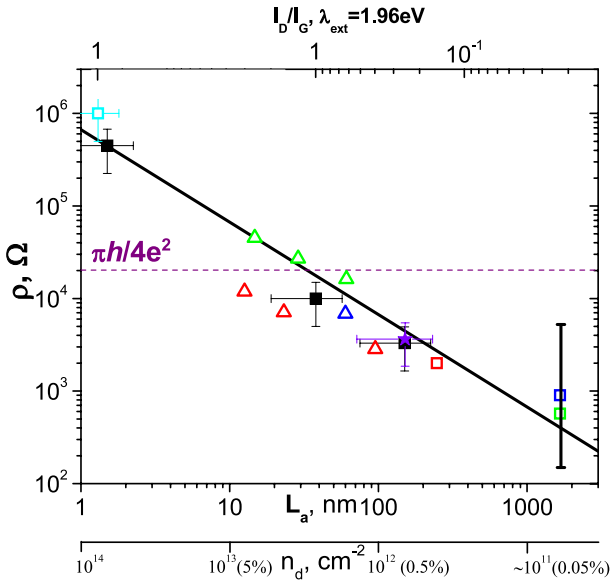

Figure 2. Graphene resistivity/sheet resistance as a function of the degree of disorder: (■)—Cu-1000, 830, 750 types, along with the fit (——) using equation (2) and multilayer graphene (Ni-830) normalized to the average number of layers (★). Literature data: □, □, □, and □ are from [9, 27, 28] and [26], respectively; △, △ are calculated using mobilities from [27] and [30] (△) by scaling with $n = 10^{12}$ cm^{-2} (see equation (3)), black line—same but calculated from mobility spread 10^3–4×10^4 cm^2 V^{-1} s^{-1} reported for exfoliated samples. Horizontal line (- - - -) is the theoretical resistivity of an undoped pristine graphene, $\pi h/4e^2$.

carrier density, n, as well as their mobility, μ. Actual contributions from each mechanism vary depending on the sample preparation history. A residual resistivity ρ_s can also contribute, $\rho = 1/en\mu + \rho_s$, [29], due to short range scatterers, but the experimental evidence suggests that its contribution is insignificant [27, 30] and thus can be omitted. In the field effect transistor geometry experiments, it was noticed that the mobility can vary significantly from sample to sample even for 'pristine' exfoliated graphene with stray n-doping on the order of $n \sim 10^{12}$ cm^{-2} on SiO_2 substrates. We used this number in calculating the resistivity where only the mobility data were given in the literature [27, 30].

Intentionally induced structural disorder and defects in graphene have been explored previously. For example, ion irradiation (with Ar^+ (90 eV) [23, 31] or with Ne^+ (500 eV) [30]) creates vacancies, hydrogen plasma treatment was also used to induce chemical modification and surface adsorption [27]. Such treatments resulted in decreased mobility in all cases; however, the physical description of the formed defects remains controversial [27, 32].

CVD grown graphene has a polycrystalline structure (supplementary data available at stacks.iop.org/Nano/22/275716/mmedia) and the D band at least partially arises from the areas close to grain boundaries, which do not correlate with the boundaries of the underlying metal catalyst. Point defects [33] also contribute to the decrease of electrical and thermal characteristics of the material. Since such defects also enhance the D band intensity, it seems logical to treat both contributions, from the grain boundaries and the point defect, without distinction and characterize them by a single effective length, L_a, of defect-free regions.

One way of describing the defects is as deep scatterers using semiclassical Boltzmann treatment [30, 34], that produce so-called midgap states and increase the resistivity proportionally to their concentration, n_d:

$$\rho = (ne\mu)^{-1} = \left(\frac{2e^2}{\pi h}\frac{n}{n_d}\ln^2(k_F R)\right)^{-1} \qquad (3)$$

where R is the radius of the defects' potential well, $k_F = \sqrt{\pi n}$ is the Fermi wavevector, e is electron charge, and h is Planck's constant. The grain boundaries in polycrystalline graphene can be treated in a similar way with a corresponding effective concentration of defects $n_d \sim 1/2RL_a$. From the slope of equation (2) and using the above mentioned assumption of $n = 10^{12}$ cm^{-2}, one obtains for the radius $R \sim 0.4$ nm, a good agreement with the dimensions of carbon cycles. We illustrate such estimated effective density of defects ($n_d = 1/2RL_a$) on the bottom axis of figure 2.

Among the alternative interpretations, one possibility includes a diminishing continuity in poor quality graphene or deposition of amorphous carbon. We did observe small pinhole defects in Cu-830 and Cu-750 samples by Auger spectroscopy (supplementary data available at stacks.iop.org/Nano/22/275716/mmedia) but their concentration is too low to explain such dramatic changes in resistivity. Another possible effect can be suggested for the role of catalyst grains but their size does not seem to be of importance here either since the grains are typically larger than L_a. Furthermore, graphene grown on Cu that had grain size varying by an order of magnitude did not affect the outcome (supplementary data available at stacks.iop.org/Nano/22/275716/mmedia). Cu-1000 graphene appears in TEM very similar to other reported samples with the average graphene domain sizes of about 250 nm [35], thus supporting our L_a estimates. Therefore, the temperature of CVD growth and not the catalyst grain size is the defining factor affecting the degree of disorder in CVD grown graphene.

2.3. Thermal conductivity

Many carbon allotropes show high thermal conductivities often exceeding the value for copper, $K \sim 400$ W m^{-1} K^{-1}. For example, diamond has a thermal conductivity of $K =$ 900–2300 W m^{-1} K^{-1}. Similarly large values were reported for highly ordered pyrolytic graphite (HOPG) in-plane $K \sim 2000$ W m^{-1} K^{-1} [36], and even higher, $K =$ 3500 W m^{-1} K^{-1}, for single wall carbon nanotubes [37].

Measuring thermal conductivity of suspended films only one atom thick is quite a challenging task and is likely the cause for a large spread in the reported room temperature values spanning over an order of magnitude (630–5300 W m^{-1} K^{-1}) even for similar quality samples (exfoliated graphene in [38, 39]). The value reported for CVD grown suspended graphene lies in between $K =$ 2500 ± 1050 W m^{-1} K^{-1} at room temperature [40]. Phonon scattering and leaking at interfaces result in a lower K for

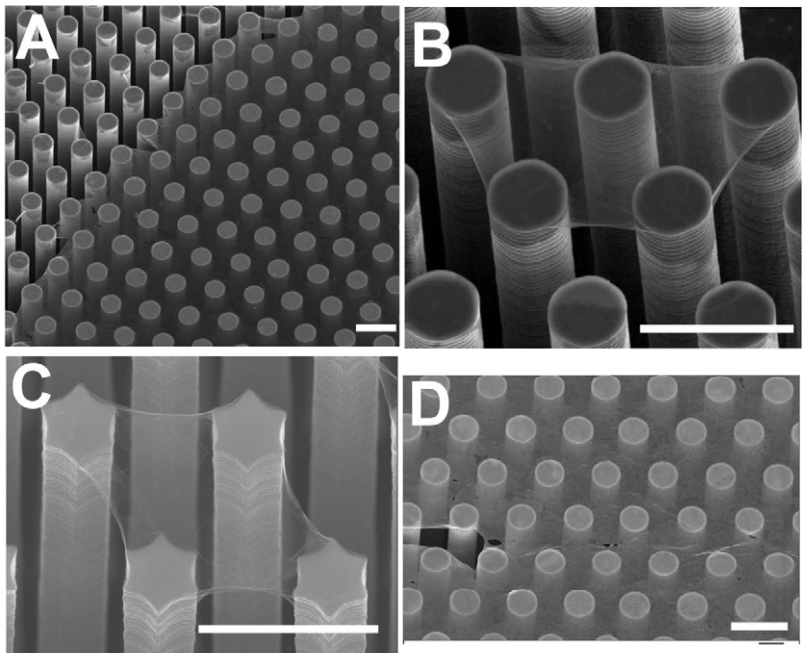

Figure 3. SEM images of suspended graphene: (A) and (B). Single layer graphene with low disorder (Cu-1000). (C) Most disordered graphene—Cu-750. (D) Multilayer graphene—Ni-830. Scale bar 5 μm. Images with ruptured graphene areas were intentionally chosen to contrast the regions with graphene. Films transferred onto smooth substrates are always continuous, while ruptured regions are occasionally observed on pillars. All measurements were performed only on continuous films.

supported graphene compared to the suspended samples; $K \sim 600$ W m^{-1} K^{-1} was reported for graphene on SiO_2 [41] and $K < 100$ W m^{-1} K^{-1} for graphene encased in SiO_2 [42].

Opposite to what is seen in metals, electrons in graphene make a minor contribution to its thermal conductivity, similar to that of graphite. Intrinsic K of graphite is limited by the anharmonic three phonon Umklapp scattering mechanism, but the actual theoretical thermal conductivity value can vary substantially due to uncertainty of the Gruneisen parameter [36, 43]. Intrinsic mean free path of phonons in graphene is greater than 1 μm and thus the thermal conductivity is highly influenced by the sample size and/or the grain size [36, 44]. Defects in the crystalline structure of graphene also contribute to the thermal conductivity decrease and significant decrease of K was predicted both for carbon nanotubes [45] and graphite [36] possessing various types of defects.

We measure thermal conductivity of graphene samples of various degree of disorder suspended on silicon pillars (see figure 3) using capabilities of the Raman instrument. The same laser beam used for Raman probing is employed to produce local heating that can be evaluated via the G band position shift [46], or from the Stokes/anti-Stokes intensity ratio:

$$\frac{I_S}{I_A} = \left(\frac{\omega_0 - \omega_G}{\omega_0 + \omega_G}\right)^4 e^{\frac{\hbar\omega_G}{kT}}. \quad (4)$$

Here $\hbar\omega_0$ is the laser excitation energy of 1.96 eV and $\hbar\omega_G$ is the energy of the G phonon, the intensity of which is monitored. The magnitude of the temperature induced shift for the G band position reported in the literature varies significantly (0.04 [40], 0.032 [47] and 0.016 [38] cm^{-1} K^{-1}) most likely because of the different temperature ranges used for the measurements. Other crucial experimental parameters include graphene absorbance at the laser wavelength, A, and the laser spot radius, a. We have measured the optical absorbance in a separate experiment and found it to be equal $\sim$2.3% for single layer graphene obtained on Cu, in agreement with the theoretical value, $\pi e^2/\hbar c$ [14].

The heat dissipation upon laser irradiation can be described by the heat diffusion equation:

$$-K\Delta T = Q + q(T_a - T) \quad (5)$$

where T_a is the ambient temperature (300 K), $Q(x, y)$—the volumetric heat source arising from laser power absorption: $Q(x, y) = \frac{P_{laser}*A}{d} I(x, y) = \frac{P_{laser}*A}{d} \frac{1}{\pi a^2} e^{-\frac{x^2+y^2}{a^2}}$, with P_{laser} the incident laser power of a Gaussian profile $I(x, y)$ with the radius $a = 0.2$ μm (corresponding to the diffraction limited spot size for the 100× objective) located at the center in between pillars. Since there is no noticeable sagging for graphene between the pillars (figure 3) its imaging is performed in the same focal plane as the pillars' tops. The thickness of the graphene sheet was taken as $d = 0.3$ nm and its absorbance, $A = 0.023$. The silicon pillars (see figure 3) act here as thermal sinks with the interfacial thermal conductance, q, for which we take a typical value found for a variety of substrate–graphene interfaces [40, 48], $qd \approx 20$ MW m^{-2} K^{-1}. Note that the exact value of q is actually of little importance since it does not have a significant effect on the calculated parameters in our geometry (supplementary available at stacks.iop.org/Nano/22/275716/mmedia). The

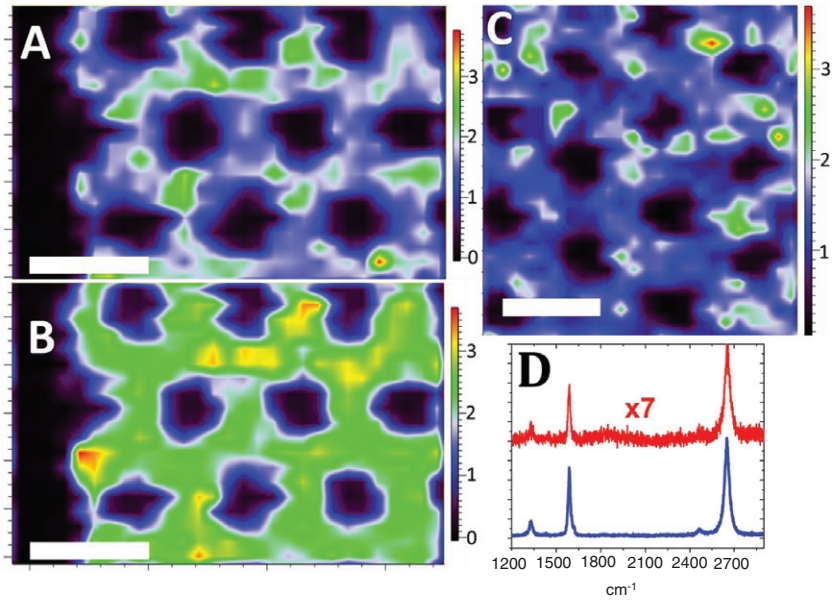

Figure 4. Raman mapping of suspended graphene on silicon pillars: (A) Stokes G band of graphene Cu-830. (B) Stokes 2D band of graphene Cu-830. (C) Stokes G band of a multilayer graphene Ni-830. (D) Raman spectra of graphene Cu-1000 for the region suspended between pillars (—) and on top of a pillar (—); the latter is multiplied by a factor of 7. Scale bar −5 μm.

effect of surrounding atmosphere and interlayer conductance for the Ni-830 sample is even less important because of a high in-plane thermal conductivity of graphene which is more than an order of magnitude higher than the interlayer conductance. Efficient contact between graphene and the pillars is clearly demonstrated by the quenched Raman signal in the pillar region (figure 4). The Raman intensity of graphene is significantly smaller on non-dielectric surfaces and is likely due to the resonant energy transfer to the substrate. The intensities of both G and 2D bands within the pillar area are noticeably decreased compared to the suspended graphene regions. Surprisingly, even for a multilayer graphene grown on Ni (Ni-830) the Raman intensity is significantly suppressed (figure 4(C)) which points to a strong optical coupling with the substrate.

Figure 5 shows the Stokes and anti-Stokes G bands measured at various laser powers at the midpoint between the pillars. The red shifting with increasing laser power in figure 5(A) is traced by the orange line and corresponds to a 2 cm^{-1} difference between the 1.7 mW (black line) and 0.32 mW (blue line) of the incident laser power. Similar shifts were observed for the anti-Stokes line (figure 5(B)), which is also of Lorentzian shape. The insets in figures 5(A) and (B) show both bands normalized by the laser power. The Stokes G band almost perfectly scales with the power, while the normalized anti-Stokes line shows pronounced enhancement illustrating the laser induced local heating. The integration times for Stokes and anti-Stokes signals were 1 and 5 min, correspondingly, which is more than sufficient for achieving a steady temperature distribution and yet is too weak for introducing additional defects. The behavior for multilayer graphene is very similar and is described in supplementary information (available at stacks.iop.org/Nano/22/275716/mmedia).

Modeling of the temperature distribution was performed by numerical solution of equation (5) for the pillar geometry as in figure 3 and the results are given in figure 5(C). Obviously, the distribution depends on the laser power, sample absorbance and its thermal conductivity. If the latter increases, the temperature does not rise as much, which is how the value of K is recovered. Low enough laser powers have to be used, especially with low conductivity Cu-750 samples because of potentially detrimental effects of local heating [49]. The calculated temperatures (and the values of K) appear different in two types of analysis: the G band shift and the anti-Stokes intensity, I_A/I_S. For the former, the average over the laser spot temperature was calculated as a function of thermal conductivity, $K : \langle T(K)\rangle = \int T(x, y, K)I(x, y)\,d\Omega$. Similarly for the latter, the anti-Stokes intensity averaged over the laser irradiated spot can be directly compared with the experiment. The effective temperature in this case, $\langle T(K)\rangle^* \sim \ln^{-1}[\langle \frac{I_S}{I_A}\rangle]$, is slightly less than $\langle T(K)\rangle$ but not significantly. The thermal conductivity of suspended graphene is higher when it is supported by a substrate, i.e. lying on pillars. It makes these regions effective thermal sinks but their effect on the extracted values of K is negligible (<10%) when the laser spot is centered in between pillars. Thus the actual value of the interface thermal conductance, q, is also of no importance (see supporting information available at stacks.iop.org/Nano/22/275716/mmedia).

Figure 6(A) shows the resulting thermal conductivity measured for the same graphene samples as a function of the degree of disorder calculated from I_D/I_G as above in the resistivity plot. The value of K determined from the G band shift (for Cu-1000 graphene) appears much higher than from the Stokes/anti-Stokes ratio but in line with previously reported results using the same approach. When using 0.04 cm^{-1} K^{-1} band calibration shift [40], the calculated conductivity is

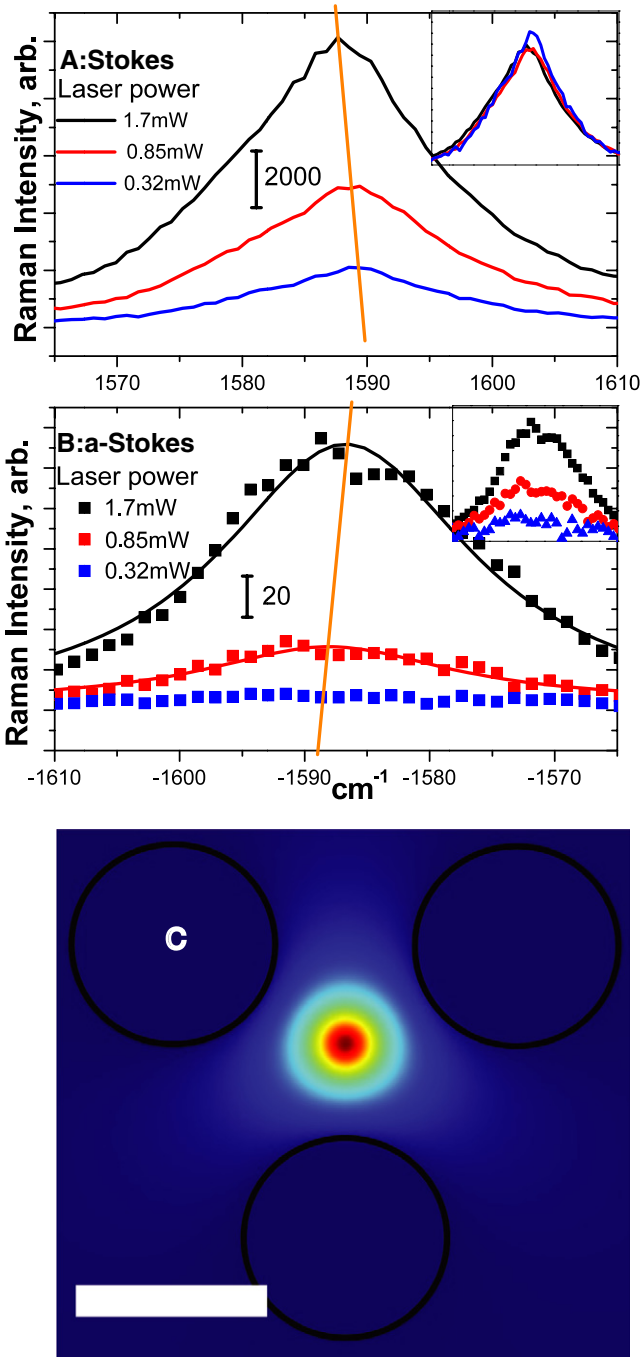

Figure 5. Stokes (A) and anti-Stokes (B) Raman G band of the Cu-1000 graphene for different incident laser powers. The orange line is a guide to the eye showing the G band red shift with laser power (heating). The insets illustrate the same data normalized by the laser power. Solid squares—experimental data; lines—Lorentzian fits. (C) Numerical solution of the temperature distribution under laser heating. Pillars are identified by three circles around the laser spot in the center. Scale bar −3 μm.

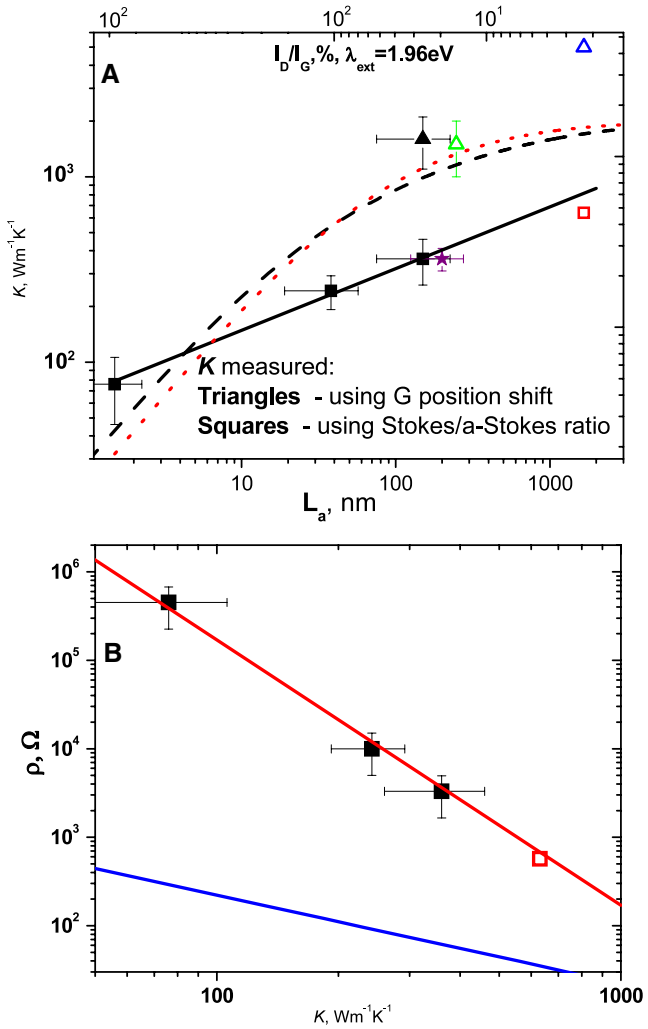

Figure 6. Thermal conductivity coefficient of graphene, K, as a function of the degree of disorder calculated from the Stokes/Anti-Stokes ratio (squares) and from the G band shift (triangles). Solid points—this work; ■—graphene type Cu-1000, Cu-830, and Cu-750; ▲—graphene type Cu-1000 calculated using G band shift 0.016–0.04 cm^{-1} K^{-1}. The point for multilayer graphene Ni-830 (★), determined using the Stokes/Anti-Stokes ratio, is slightly shifted for clarity. Open symbols from △ [39], △ [40], and △ [38]. The solid black line shows $K \sim L_a^{1/3}$ correlation, while the analytical model of equation (6) is shown by the dashed line (supplementary data available at stacks.iop.org/Nano/22/275716/mmedia). The dotted line shows the thermal conductivity dependence on defect concentrations. See text for details. (B) Correlation between the electrical resistivity, ρ, and thermal conductivity, K, of graphene of different degree of disorder; (—) the power law correlation between the two, $\rho \sim K^{-3}$, along with the Wiedemann–Franz law for metals (—).

$K \sim$ 1200 W m^{-1} K^{-1} (see supplementary data available at stacks.iop.org/Nano/22/275716/mmedia). Higher absorbance, such as $A = 0.13$ used in [38], would lead to even higher extracted conductivity, $K \sim$ 2100–5300 W m^{-1} K^{-1}, among the highest reported. When explaining a similar discrepancy for temperature readout using the G band shift and Stokes/anti-Stokes ratio, Chae *et al* have suggested in a recent paper [47] that localized heating corresponds to nonequilibrium conditions and cannot be directly compared to uniform heating. The extracted temperature is higher for nonequilibrium local heating which translates to a lower value of K. Nevertheless, there is no clear understanding of the discrepancy as other studies report that the temperature calculated from the Stokes/anti-Stokes ratio in a similar experiment was close to the electronic temperature measured

by thermal emission [50, 51], at least for temperatures higher than 500 K, i.e. pointing to quasi-equilibrium conditions.

Other factors such as adsorption/desorption of dopants (e.g. water) during cooling/heating and the stress induced shift (see supplementary data available at stacks.iop.org/Nano/22/275716/mmedia) could interfere with a purely thermal G band shift and thus contribute to an apparently higher K. Because of that and since only low laser power measurements are possible for highly disordered samples (like Cu-750), we focus in figure 6 on measurements using the I_S/I_A ratio.

As figure 6 demonstrates, the thermal conductivity declines with increasing degree of disorder in graphene but is much slower than its electrical conductivity. Even for substantially disordered samples with very small domain size, $L_a \sim 1$ nm, the thermal conductivity coefficient exceeds that of amorphous carbon (<1 W m^{-1} K^{-1}) by an order of magnitude. Similar to figure 2, the value of K for exfoliated graphene samples [39], scaled in accordance with the ratio $I_D/I_G \sim 0.01$, follows the same trend and so does the multilayer graphene of the same quality as estimated using the Stokes/anti-Stokes ratio (figure 6(A), pink star). The apparent trend seems to follow a power law, $K \sim L_a^{1/3}$, for which there is no theoretical explanation.

The current model of Klemens [52] mimics the thermal conductivity in graphitic materials by integrating the phonon spectrum altered because of grains that introduce a size dependent cutoff frequency ω_G:

$$K = K_0 \frac{1}{2} \frac{\ln(\frac{\omega_m^2+\omega_G^2}{\omega_c^2+\omega_G^2})}{\ln(\frac{\omega_m}{\omega_c})}. \quad (6)$$

Here the maximum cutoff and the low bound cutoff phonon frequencies were taken $\omega_m \sim 3 \times 10^{14}$ s^{-1} and $\omega_c \sim 2.5 \times 10^{13}$ s^{-1}, respectively, while the thermal in-plane conductivity of HOPG in the absence of grains was taken as $K_0 = 2000$ W m^{-1} K^{-1}, which provides a reasonable agreement with experimental data for temperatures $T > 300$ K [36]. Some recent improvements to this theory allow separate treatment of LA and TA phonons [44] but it has not changed dramatically the outcome of equation (6). Equation (6) predicts a weak dependence of K on L_a. Following the Klemens' scaling for $\omega_G \sim L_a^{-1/2}$, we find the best fit with $\omega_G \sim 3 \times 10^{10} L_a^{1/2}$ s^{-1} (see figure 6(A), dashed line), which changes faster than the experimental variation. One way to circumvent this is by realizing that the effective grain size, L_a, represents an average of some distribution function of their dimensions and thus equation (6) has to be weighted accordingly. Alternatively, one can convolute it into an effective weaker dependence of ω_G on L_a to get a better fit. A similar dependence can be derived for point defects which, according to Klemens [36], shorten the phonon mean free path by $(1 + \omega/\omega_0)$ to give:

$$K = K_0 \left[1 - \frac{\ln(\frac{\omega_m+\omega_0}{\omega_c-\omega_0})}{\ln(\frac{\omega_m}{\omega_c})}\right]. \quad (7)$$

The characteristic scattering frequency scales linearly with L_a, $\omega_0 = 6.2 \times 10^9 L_a$ (s^{-1}), where the defect concentration was estimated as above, $n_d \sim 1/2RL_a$. Equation (7) also leads to a weak dependence of K on L_a (figure 6(A), dotted line) almost identical to equation (6), i.e. does not recover the apparent power law dependence, $K \sim L_a^{1/3}$.

Molecular modeling offers completely different scaling for the thermal conductivity with the size of carbon nanostructured materials. Non-equilibrium molecular dynamics simulations by Guo *et al* [53] suggested a power (rather than logarithmic) dependence of $K \sim L^\beta$ on the length, L, of graphene nanoribbons and nanotubes. The power β varied in the range $\beta \sim 1/4$–$1/2$ depending on the nanotube chirality and graphene nanoribbon boundary (armchair or zigzag). Verifying such a power law for our data suggests that $K \sim L_a^{1/3}$. Surprisingly this trend fits our data and those for mechanically exfoliated graphene.

Figure 6(B) combines the data of figures 2 and 6(A) by showing the electrical resistivity as a function of the thermal conductivity. The apparent correlation, $\rho K^3 = \text{const}$, obviously agrees with the above established individual power laws, $\rho \sim L_a^{-1}$ and $K \sim L_a^{1/3}$, but is free of any inaccuracies in defining L_a. The Wiedemann–Franz law, $\rho K = LT \sim 7.5 \times 10^{-5}$ W Ω K^{-1}, is shown for comparison and represents a similar dependence for metals. In order to scale with bulk resistivity, the thickness of graphene was taken as $d = 0.3$ nm, as above. The Wiedemann–Franz law can be also treated as identifying a pure electronic contribution to the thermal conductivity. In this case it indicates that for all samples the phonon contribution overwhelms the electronic one by orders of magnitude, especially the lower-quality ones. It is interesting to note that the two power law curves would formally converge when $K \sim 2000$ W m^{-1} K^{-1}, i.e. close to K_0, and $\rho \sim 20$ Ω, which almost coincides with the anticipated value for the theoretical longitudinal acoustic (LA) phonon scattering limited mobility, $\mu \sim 2 \times 10^5$ cm^2 V^{-1} s^{-1} [28], and the doping level of $n \sim 10^{12}$ cm^{-2}.

3. Conclusions

We have shown that CVD growth of a continuous graphene monolayer on Cu can be performed at temperatures as low as 750 °C. Despite structural defects induced by lowering the temperature of growth, such monolayer graphene possesses high electrical and thermal conductivities that together with low temperature processing make it very attractive in numerous applications where good thermal management, transparency and conductance are desired. The thermal conductivities measured from the temperature dependence of the G band position result in almost an order of magnitude (seven-fold) greater values compared to those calculated from anti-Stokes intensities. Structural disorder, as evaluated from the Raman G band and D band ratio (I_G/I_D), gradually increases with lowering the deposition temperature and can be related to a decreasing size of monocrystalline graphene domains, L_a. The corresponding decline in the electrical conductivity is close to a linear function of L_a, while the thermal conductivity (as evaluated from the relative anti-Stokes intensity) is a much weaker function of L_a, with an apparent power dependence $K \sim L_a^{1/3}$.

Acknowledgments

IV is a Eugene P Wigner Fellow at the Oak Ridge National Laboratory, managed by UT-Battelle, LLC, for the US Department of Energy under Contract DE-AC05-00OR22725. A portion of this research was conducted at the Center for Nanophase Materials Sciences, which is sponsored at Oak Ridge National Laboratory by the Office of Basic Energy Sciences, US Department of Energy. TEM is operated at ORNL's Shared Research Equipment (SHaRE) User Facility, which is sponsored by the Office of Basic Energy Sciences, US Department of Energy. PFF and SD were supported as part of the Fluid Interface Reactions, Structures and Transport (FIRST) Center, an Energy Frontier Research Center funded by the US Department of Energy, Office of Science, Office of Basic Energy Sciences under Award Number ERKCC61.

References

[1] Novoselov K S, Geim A K, Morozov S V, Jiang D, Zhang Y, Dubonos S V, Grigorieva I V and Firsov A A 2004 *Science* **306** 666–9
[2] Zhu Y, Murali S, Cai W, Li X, Suk J W, Potts J P and Ruoff R S 2010 *Adv. Mater.* **22** 3906–24
[3] Avouris P 2010 *Nano Lett.* **10** 4285–94
[4] Geim A K and Novoselov K S 2007 *Nat. Mater.* **6** 183–97
[5] Geim A K 2009 *Science* **324** 1530–4
[6] Bae S *et al* 2010 *Nat. Nanotechnol.* **5** 574
[7] Wang X, Fulvio P, Baker G, Veith G, Unocic R, Mahurin S, Chi M and Dai S 2010 *Chem. Commun.* **46** 4487–9
[8] Li X *et al* 2009 *Science* **324** 1312–4
[9] Li X, Zhu Y, Cai W, Borysiak M, Han B, Chen D, Piner R D, Colombo L and Ruoff R S 2009 *Nano Lett.* **9** 4359–63
[10] Lee Y, Bae S, Jang H, Jang S, Zhu S-E, Sim S H, Song Y, Hong B H and Ahn J-H 2010 *Nano Lett.* **10** 490–3
[11] Levendorf M P, Ruiz-Vargas C S, Garg S and Park J 2009 *Nano Lett.* **9** 4479–83
[12] Reina A, Theile S, Jia X, Bhaviripudi S, Dresselhaus M S, Schaefer J A and Kong J 2009 *Nano Res.* **2** 509–16 and references therein
[13] Dresselhaus M S, Jorio A, Hofmann M, Dresselhaus G and Saito R 2010 *Nano Lett.* **10** 751–8
[14] Nair R R, Blake P, Grigorenko A N, Novoselov K S, Booth T J, Stauber T, Peres N M R and Geim A K 2008 *Science* **320** 1308
[15] Bhaviripudi S, Jia X, Dresselhaus M S and Kong J 2010 *Nano Lett.* **10** 4128–33
[16] Tuinstra F and Koenig J L 1970 *J. Chem. Phys.* **53** 1126
[17] Ferrari A C 2007 *Solid State Commun.* **143** 47–57
[18] Pimenta M A, Dresselhaus G, Dresselhaus M S, Cancado L G, Jorio A and Saito R 2007 *Phys. Chem. Chem. Phys.* **9** 1276–91
[19] Ferrari A C *et al* 2006 *Phys. Rev. Lett.* **97** 187401
[20] Casiraghi C, Pisana S, Novoselov K S, Geim A K and Ferrari A C 2007 *Appl. Phys. Lett.* **91** 233108
[21] Yan J, Zhang Y, Kim P and Pinczuk A 2007 *Phys. Rev. Lett.* **98** 166802
[22] Das A *et al* 2008 *Nat. Nanotechnol.* **3** 210
[23] Ferreira E H, Moutinho M V O, Stavale F, Lucchese M M, Capaz R B, Achete C A and Jorio A 2010 *Phys. Rev.* B **82** 125429
[24] Knight D S and White W 1989 *J. Mater. Res.* **4** 385
[25] Cancado L G, Takai K, Enoki T, Endo M, Kim Y A, Mizusaki H, Jorio A, Coelho L N, Magalhaes-Paniago R and Primenta M A 2006 *Appl. Phys. Lett.* **88** 163106
[26] Turchanin A, Beyer A, Nottbohm C T, Zhang X, Stosch R, Sologubenko A, Mayer J, Hinze P, Weimann T and Golzhauser A 2009 *Adv. Mater.* **21** 1233–7
[27] Ni Z H *et al* 2010 *Nano Lett.* **10** 3868–72
[28] Chen J H, Jang C, Xiao S, Ishigami M and Fuhrer M S 2008 *Nat. Nanotechnol.* **3** 206–9
[29] Jang C, Adam S, Chen J H, Williams E D, Das Sarma S and Fuhrer M S 2008 *Phys. Rev. Lett.* **101** 146805
[30] Chen J-H, Cullen W G, Jang C, Fuhrer M S and Williams E D 2009 *Phys. Rev. Lett.* **102** 236805
[31] Luccese M M, Stavale F, Martins Ferreira E H, Vilani C, Moutinho M V O, Capaz R B, Achete C A and Jorio A 2010 *Carbon* **48** 1592–7
[32] Wehling T O, Yuan S, Lichtenstein A I, Geim A K and Katsnelson M I 2010 *Phys. Rev. Lett.* **105** 056802
[33] Yu Q *et al* 2010 arXiv:1011.4690v1
[34] Stauber T, Peres N M R and Guinea F 2007 *Phys. Rev. Lett.* **76** 205423
[35] Huang P Y *et al* 2011 *Nature* **469** 389
[36] Klemens P G and Pedraza D F 1994 *Carbon* **32** 735–41
[37] Pop E, Mann D, Wang Q, Goodson K and Dai H 2006 *Nano Lett.* **6** 96–100
[38] Balandin A A, Ghosh S, Bao W, Calizo I, Teweldebrhan D, Miao F and Lau C N 2008 *Nano Lett.* **8** 902–7
[39] Faugeras C, Faugeras B, Orlita M, Potemski M, Nair R R and Geim A K 2010 *ACS Nano* **4** 1889–92
[40] Cai W, Moore A L, Zhu Y, Li X, Chen S, Shi L and Ruoff R S 2010 *Nano Lett.* **10** 1645–51
[41] Seol J H *et al* 2010 *Science* **328** 213–6
[42] Jang W, Chen Z, Bao W, Lau C N and Dames C 2010 *Nano Lett.* **10** 3903–13
[43] Nika D L, Pokatilov E P, Askerov A S and Balandin A A 2009 *Phys. Rev.* B **79** 155413
[44] Nika D L, Ghosh S, Pokatilov E P and Balandin A A 2009 *Appl. Phys. Lett.* **94** 203103
[45] Che J, Cagin T and Goddard W A III 2000 *Nanotechnology* **11** 65–9
[46] Bonini N, Lazzeri M, Marzari N and Mauri F 2007 *Phys. Rev. Lett.* **99** 176802
[47] Chae D-H, Krauss B, von Klitzing K and Smet J H 2010 *Nano Lett.* **10** 466–71
[48] Mak K F, Lui C H and Heinz T F 2010 *Appl. Phys. Lett.* **97** 221904
[49] Krauss B, Lohmann T, Chae D-H, Haluska M, von Klitzing K and Smet J H 2009 *Phys. Rev.* B **79** 165428
[50] Freitag M, Chiu H-Y, Steiner M, Perebeinos V and Avouris P 2010 *Nat. Nanotechnol.* **5** 497
[51] Berciaud S, Han M Y, Mak K F, Brus L E, Kim P and Heinz T F 2010 *Phys. Rev. Lett.* **104** 227401
[52] Klemens P G 2001 *Int. J. Thermophys.* **22** 265–75 and references therein
[53] Guo Z, Zhang D and Gong X-G 2009 *Appl. Phys. Lett* **95** 163103